Supporting Information

Synergistic photothermal and photochemical partial oxidation of methane over noble metals incorporated in mesoporous silica

Haoyang Jiang,[†] Xiaobo Peng,[‡] Akira Yamaguchi,[†] Takeshi Fujita,[¶] Hideki Abe,[‡] and Masahiro Miyauchi[*,†]

[†]Department of Materials Science and Engineering, Tokyo Institute of Technology, 2-12-1 Ookayama, Meguro, Tokyo 152-8552, Japan

[‡]National Institute for Materials Science (NIMS), 1-1 Namiki, Tsukuba, Ibaraki 305-0044, Japan

[¶]School of Environmental Science and Engineering, Kochi University of Technology, 185 Miyanokuchi, Tosayamada, Kami, Kochi 782-8502, Japan

*Corresponding author: mmiyauchi@ceram.titech.ac.jp

Note 1. Catalyst preparation

Aqueous ammonia, hydrochloric acid, and metal chlorides including $RhCl_3 \cdot 3H_2O$, $PdCl_2$, and $H_2PtCl_6 \cdot 6H_2O$, were purchased from Fujifilm Wako Co., Ltd. $RuCl_3 \cdot 3H_2O$ and cetyltrimethylammonium bromide (CTAB) were purchased from Kanto Chemical Co., Inc. Tetraethoxysilane (TEOS) and commercial MCM-41 powder were purchased from Sigma-Aldrich, Inc.

Mesoporous silica (MCM-41) incorporated with noble metals, denoted as M/MCMs (M = Ru, Rh, Pd, and Pt) was prepared via a one-pot precipitation process. In detail, 0.13 mmol of metal chloride was dissolved in 30 mL ultrapure water. In particular, $PdCl_2$ was pre-dissolved in a small amount of hot hydrochloric acid before this operation. Then, 1.5 g of CTAB template reagent, 45 mL of ethanol, and 35 mL of aqueous ammonia were added under magnetic stirring to form a clear colloidal solution. Precipitation generated after 13 mmol of TEOS was added dropwise to the solution. The slurry was stirred continuously at room temperature for 24 h. Afterward, the precipitation was collected by centrifugation, washed by pure water, and dried at 378 K in an oven. The obtained powder was calcinated in air at 823 K for 5 h to remove the organic template, and subsequently reduced under a 5% H_2-Ar flow at 723 K for 2 h to obtain the final product. The loading amount of metals was determined by inductively coupled plasma mass spectrometry (ICP-MS), and the result is shown as follows. The reason that measured M/SiO_2 ratios were much lower than the input amounts are probably due to the limited adsorbing capacity of silica framework toward noble metal ions.

Catalyst	Input M/SiO_2 mol%	Measured M/SiO_2 mol%
Rh/MCM		0.44
Pd/MCM		0.66
Ru/MCM	1	0.61
Pt/MCM		0.52

Note 2. Catalyst characterization

The wide-angle XRD patterns in the 2θ range of 10º–90º and SAXS patterns in the 2θ range of 0º–8º were measured using a Rigaku SmartLab diffractometer with a D/teX Ultra detector. The TEM and STEM images were taken by a JEOL JEM-2010F TEM and a JEOL JEM-2100F TEM/STEM, respectively. The degrees of metal dispersion were measured with a H_2 pulse adsorption method at 308 K using an AutoChem II 2920 automated catalyst characterization system equipped with a thermal conductivity detector (TCD). The UV-vis DRS were recorded by a JASCO V-670 spectrometer in the wavelength range of 200–800 nm with a $BaSO_4$ reference.

Note 3: Catalytic performance evaluation system

The photocatalytic reactions were performed in a flow fixed-bed reactor (Heat Chamber Type-1000 °C, S.T. Japan, Inc.). A quartz window was fixed in the screw cap of the reactor. A cylindrical ceramic cup (4.8-mm inner diameter, 2-mm depth) was used to carry an 8-mg catalyst sample, which was compressed to 1 mm in thickness using a tailored pushrod. The reactant gas (1% CH_4 + 0.5% O_2 + 98.5% Ar) was fed into the reactor at a flow rate of at 10 cm^3 min^{-1} under standard conditions through a mass flow controller (SEC-E40, Horiba, Ltd.). The sample was irradiated by a 200-W Hg-Xe lamp through the quartz window. A circulating cooling water system (LTC-450A, As One Corporation) was connected to the reactor in order to alleviate the heating effect of the thermal radiation from the light source. The output gas was quantitively analyzed using an Agilent 490 micro gas chromatograph (μGC) online system equipped with multiple TCD channels. The conversions of CH_4 and O_2 (X_{CH_4} and X_{O_2}) and the yields of CO, CO_2, H_2, and H_2O (Y_{CO}, Y_{CO_2}, Y_{H_2}, and Y_{H_2O}) were calculated using Equations S1–S6:

$$X_{CH_4} = 1 - \frac{\varphi(CH_4)}{\varphi_0(CH_4)} \#(S1)$$

$$X_{O_2} = 1 - \frac{\varphi(O_2)}{\varphi_0(O_2)} \#(S2)$$

$$Y_{CO} = \frac{\varphi(CO)}{\varphi_0(CO)} \#(S3)$$

$$Y_{CO_2} = \frac{\varphi(CO_2)}{\varphi_0(CH_4)} \#(S4)$$

$$Y_{H_2} = \frac{\varphi(H_2)}{2\varphi_0(CH_4)} \#(S5)$$

$$Y_{H_2O} = \frac{\varphi(H_2O)}{2\varphi_0(CH_4)} \#(S6)$$

where $\varphi_0(CH_4)$ and $\varphi_0(O_2)$ are initial concentrations, and $\varphi(CH_4)$, $\varphi(O_2)$, $\varphi(CO)$, $\varphi(CO_2)$, $\varphi(H_2)$, and $\varphi(H_2O)$ are output concentrations. The selectivity of CO (S_{CO}) was calculated by Equation S7:

$$S_{CO} = \frac{\varphi(CO)}{\varphi_0(CH_4) - \varphi(CH_4)} \#(S7)$$

The conversion rate of CH_4 (r_{CH_4}) and generation rate of CO (r_{CO}) were calculated by Equation S8 and Equation S9, respectively:

$$v_{CH_4} = [\varphi_0(CH_4) - \varphi(CH_4)]q/V_m \#(S8)$$

$$r_{CO} = \varphi(CO)q/V_m \#(S9)$$

where q and V_m are the gas flow rate and molar volume (22.4 L/mol at 273 K and at 100 kPa), respectively. A stepped temperature program (423–973 K, 50-K intervals) was used to investigate the dependence of reactant conversions and product yields on the temperature. A constant-temperature

program that lasted for 20 h was used to test the durability of the catalyst. The instantaneous TOF was given by Equation 2.10

$$\text{TOF} = \frac{r_{CH_4}}{N \cdot D} \#(S10)$$

where r_{CH_4}, N, and D represent the conversion rate of CH_4, the total mole number of metal, and the degree of metal dispersion, respectively. The TON_{20h} is the integral of TOF over time. The surface temperature under UV irradiation was measured using an infrared thermometer (TMHX-CE0500, Japan Sensor Corporation).

Note 4: Determination of quantum yields and action spectra

The action spectra were determined by measuring the photocatalytic activities using a series of long-wave pass filters (400, 385, 350, 325, 300, 275, and 250 nm) to limit the incident wavelengths. The mole number of photons received by the photocatalyst when using a long-wave pass filter per unit time (N_{photon}) is given by Equation S11:

$$N_{photon} = \frac{1}{N_A} \int_{200\,nm}^{800\,nm} \frac{\lambda P(\lambda) S}{hc} (l'/l)^2 \, d\lambda \#(S11)$$

where $P(\lambda)$ represents the spectral power density distribution recorded by a Ushio USR-45 spectroradiometer; S represents the cross-sectional area of the sample cup; l' and l are the irradiation distances in the power density distribution measurement and the photocatalytic reaction (herein, 16 and 2 cm), respectively; and h, c, and N_A are Planck's constant, the velocity of light, and Avogadro's constant respectively. The average quantum yields of CH_4 consumption (Φ_{CH_4}) and CO formation (Φ_{CO}) using different filters are obtained using Equation S12:

$$\Phi = \frac{r_{light} - r_{dark}}{N_{photon}} \times 100\% \#(S12)$$

where r_{light} and r_{dark} refer to the reaction rates of CH_4 or CO under irradiation and dark conditions, respectively.

Note 5: Methane reforming over semiconductor-based photocatalysts

In the present study, we exclude the effect of the optical absorption of support materials since the MCM-41 is an ultrawide gap insulator. By contrast, our group also found that the band-gap excitation of the semiconductor was the dominant trigger to initiate DRM using a metal-loaded semiconductor such as $SrTiO_3$ and Ta_2O_5.[1,2] We speculate that the band-gap excitation and hot carrier generation compete in these semiconductor-based systems and depend on the type of methane conversion reactions such as POM, DRM, and STM. Indeed, the bandgap excitation was dominant in metal-loaded $SrTiO_3$ and Ta_2O_5, especially in the DRM reaction, while the hot carrier generation contributed to POM in the present MCM-41 and ultrawide-gap $Sr_2Ta_2O_7$[3] cases. Controlling the contribution of the band-gap excitation of metal oxide or hot carrier excitation of metal nanoparticles is very important in developing the selective methane conversion photocatalyst. This topic is now under investigation and will be reported elsewhere.
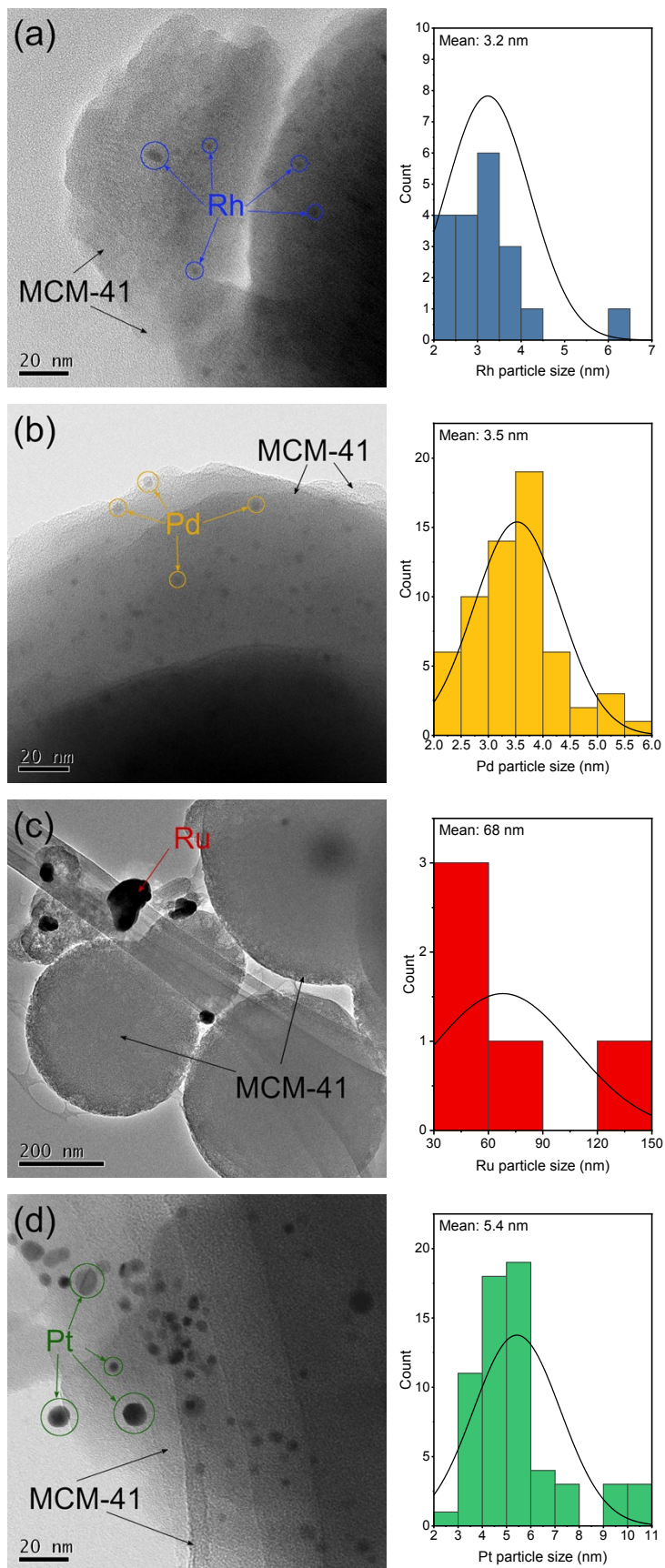
Supplementary Figures

Fig. S1 TEM images and metal particle distribution of (a) Rh/MCM, (b) Pd/MCM, (c) Ru/MCM, and (d) Pt/MCM.
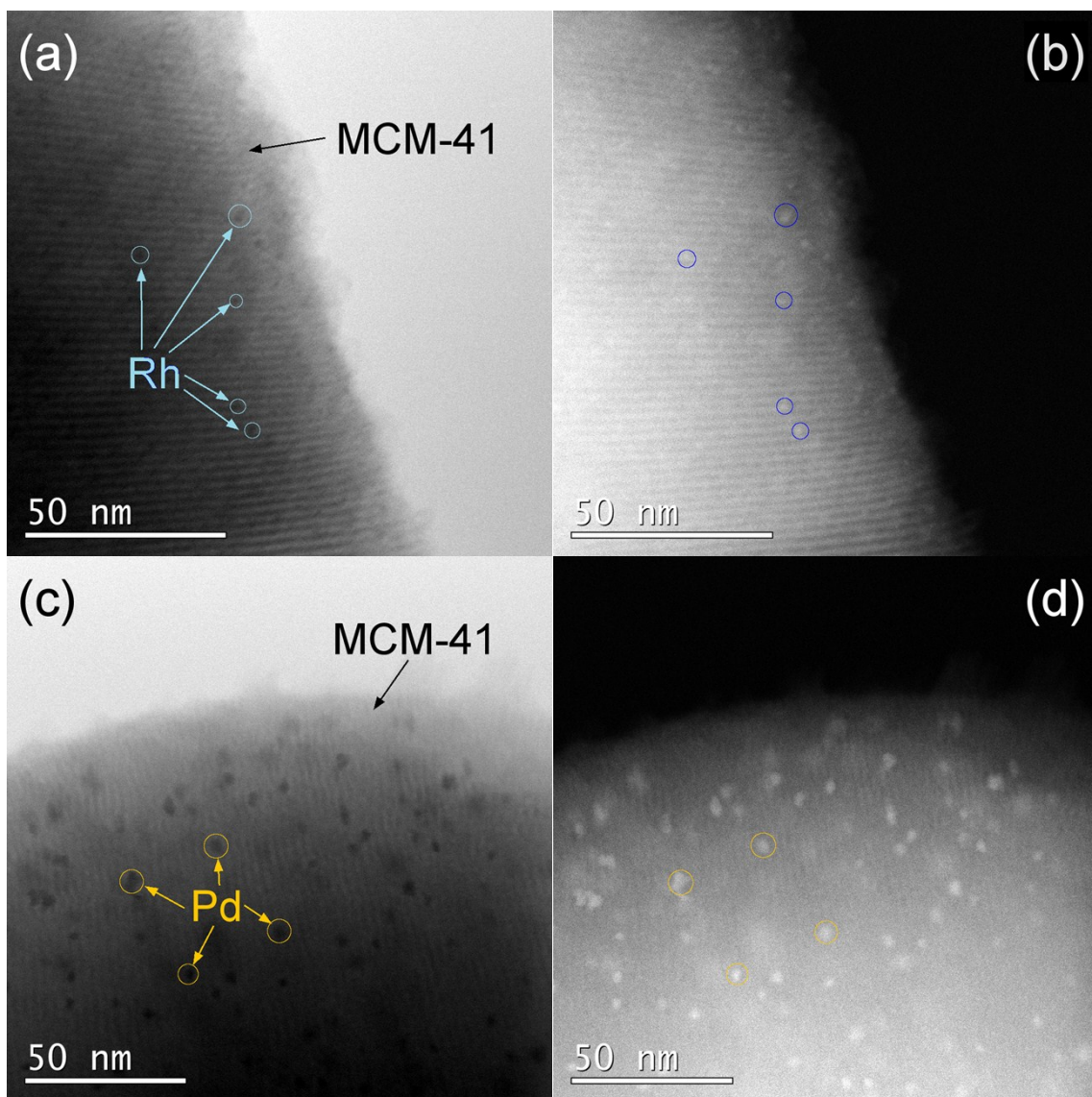
8

Fig. S2 STEM images of (a, b) Rh/MCM and (c, d) Pd/MCM along the [110] direction, in which a, c are bright-field images, and b, d are dark-field images.
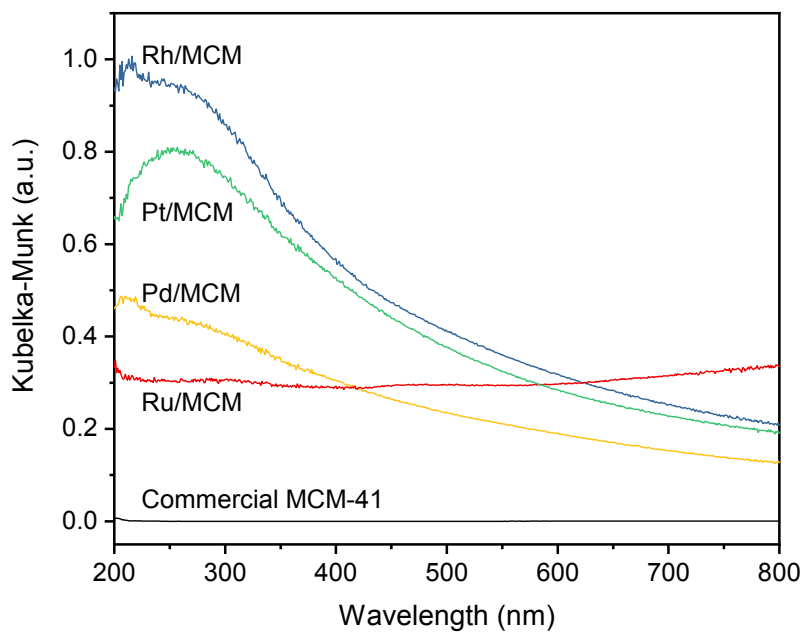
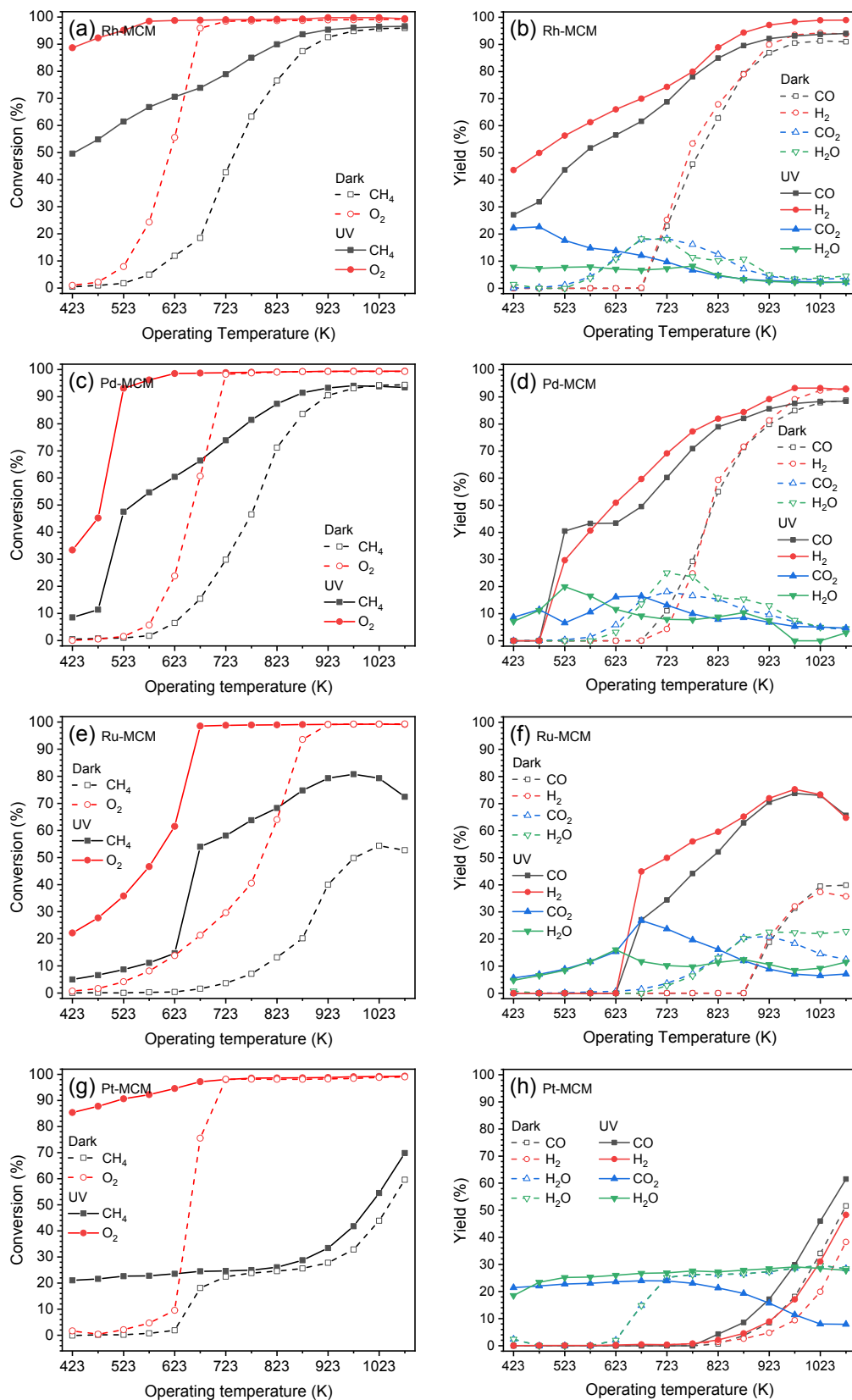**Fig. S3** UV-vis spectra of M/MCMs (M = Rh, Pd, Ru, and Pt) and commercial MCM-41.

Fig. S4 Temperature-dependent conversions of CH_4, O_2, and yields of CO, H_2, CO_2, H_2O over (a, b) Rh/MCM, (c, d) Pd/MCM, (e, f) Ru/MCM, and (g, h) Pt/MCM under dark and UV irradiation conditions.
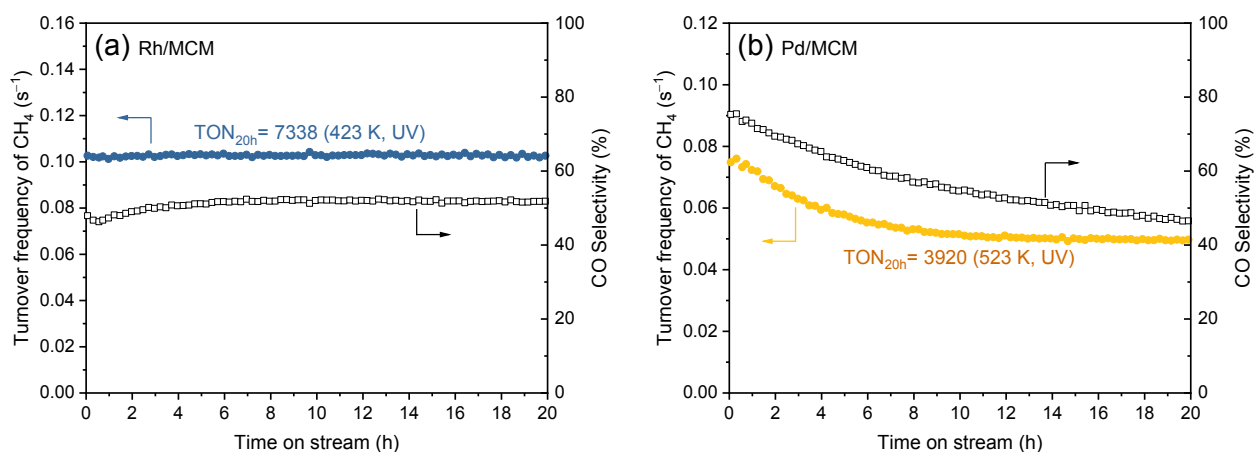
11

Fig. S5 20-h durability tests of (a) Rh/MCM at 423 K and (b) Pd/MCM at 523 K, under UV irradiation. Rh/MCM exhibited remarkable photocatalytic stability in which the turnover frequency (TOF) for CH_4 stayed in the range 0.101–0.103 s^{-1} with a steady output of CO whose selectivity was in the range 46%–52%. Pd/MCM showed worse durability than Rh/MCM in that a rapid deactivation occurred in the first several hours but subsequently tended to be stable. In the entire test, the TOF of CH_4 decreased from 0.075 to 0.050 s^{-1}, and the CO selectivity decreased from 75% to 46%. Based on these results, high turnover numbers (TONs) for CH_4 were obtained using both Rh and Pd/MCMs, which were 7388 and 3920, respectively. Rh/MCM was more stable than Pd/MCM. Herein, the primary reason for the inactivation of Pd/MCM is considered the phenomenon of carbon deposition. A previous study suggested the carbon deposition rate is in the order Ni > Pd > Rh > Ru > Pt.[1] It means that Pd active sites are more easily to be blocked with carbon species, which results in worse long-term stability than the Rh case. Additionally, the following table gives the comparison of TOF/TON between the conditions with and without UV irradiation. Evidently, both long-term stability and high performance can be acquired at a moderate operating temperature under irradiation conditions.

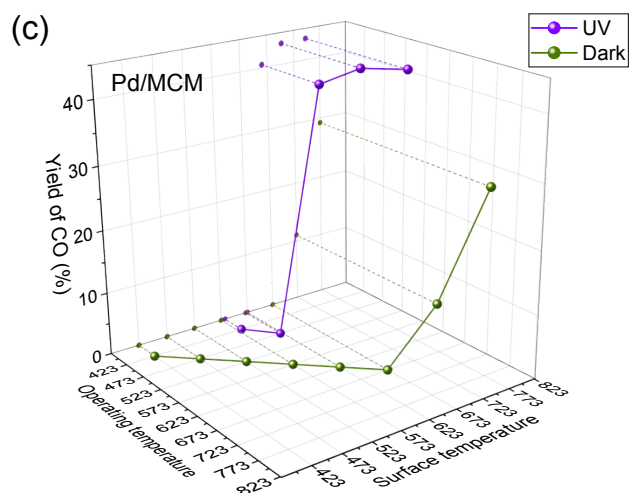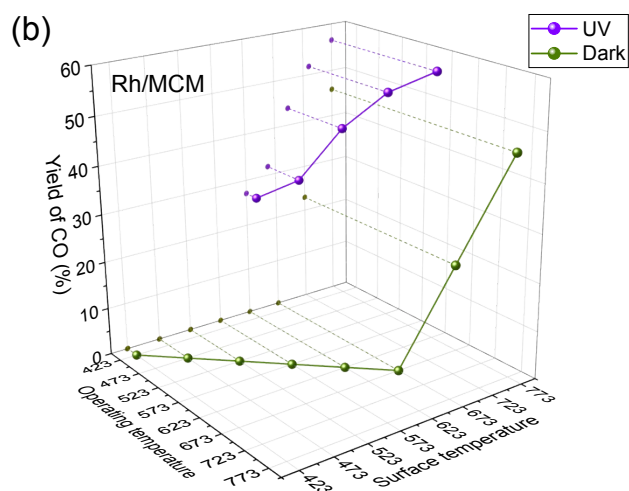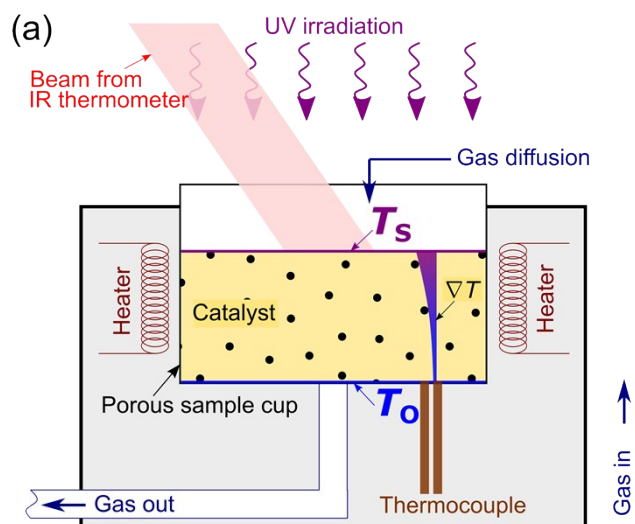| Catalyst	Condition	Operating Temperature (K)	Initial TOF (s^{-1})	Final TOF (s^{-1})	TON
Rh/MCM	Dark	723	0.100	0.100	7194
	UV	423	0.103	0.103	7338
Pd/MCM	Dark	773	0.062	0.041	3283
	UV	523	0.075	0.050	3920

Fig. S6 (a) Measurement of the surface temperature (T_S) and the operating temperature (T_O) of a catalyst bed; ∇T represents the temperature gradient. 3-D plots of the yield of CO over (b) Rh/MCM and (c) Pd/MCM as a function of operating temperature and surface temperature, under the dark conditions and UV irradiation.
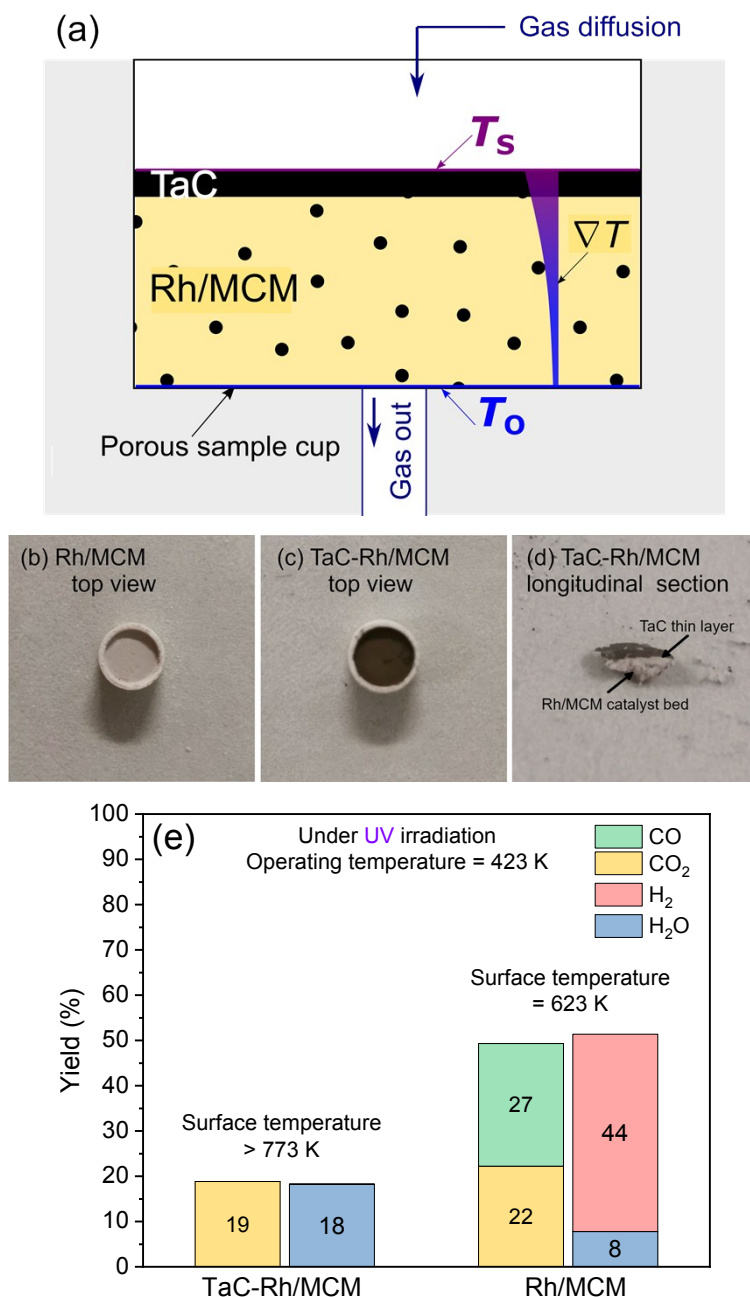
Fig. S7 Tantalum carbide (TaC) is an effective photothermal material proposed by our previous study.[3] To verify the influence of temperature gradients, as shown in panel (a), we placed a thin layer of TaC on the top of a Rh/MCM catalyst bed (denoted TaC-Rh/MCM), and tested the catalytic performance under UV irradiation. Photographs in panel (b), (c), and (d) are the top view of Rh/MCM, the top view of TaC-Rh/MCM, and the longitudinal section of TaC-Rh/MCM, respectively. In this case, Rh/MCM catalyst can hardly receive photons. Instead, TaC layer converts photon energy to heat, and transports the heat down to the catalyst bed. As shown in panel (e), at the operating temperature of 423 K, TaC-Rh/MCM showed much stronger photothermal effect than Rh/MCM, with a surface temperature exceeding 773 K. However, the catalytic activity of TaC-Rh/MCM was limited, and the generation of syngas was negligible. This result does not only exclude the contribution of temperature gradients to syngas evolution, but also demonstrate that the photothermal effect was not a determining factor. It is necessary to expose the catalyst bed to the light directly.
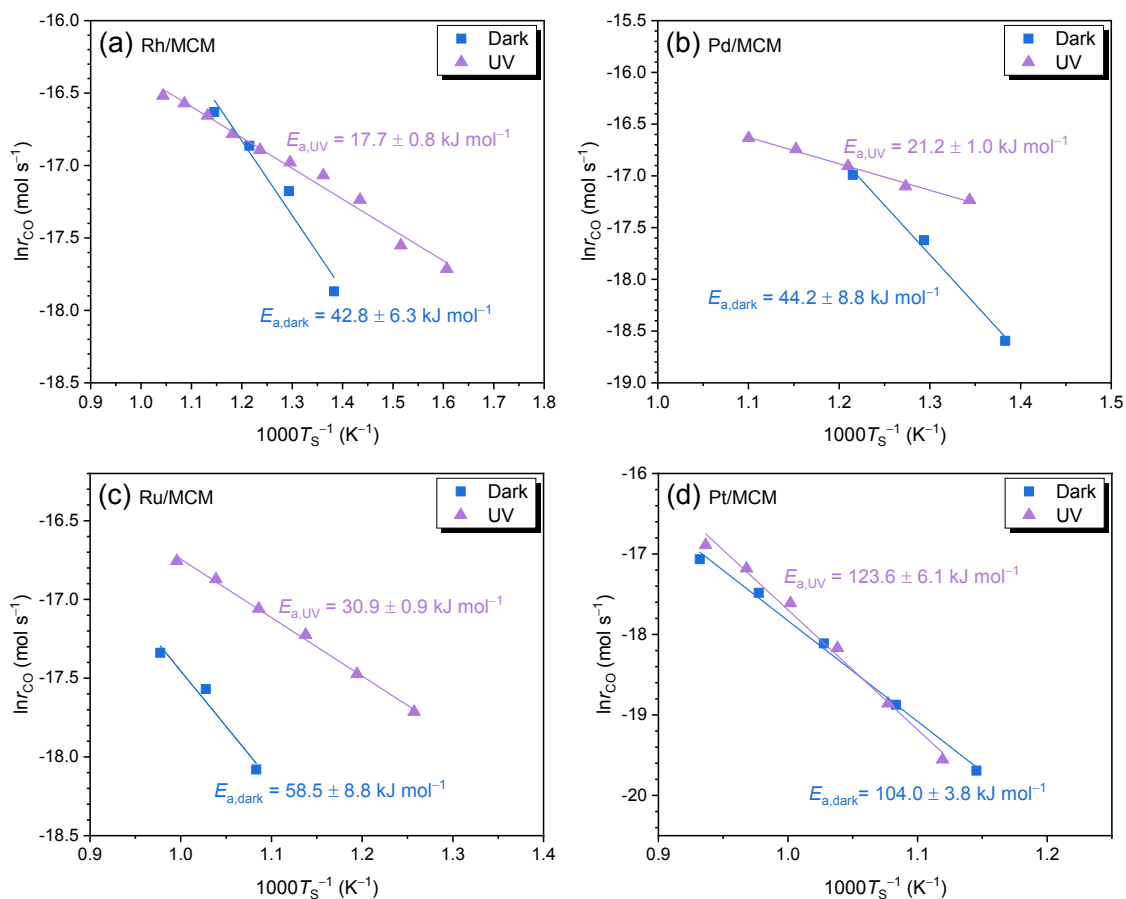
14

Fig. S8 The Arrhenius plots and estimation of apparent active energy for CO generation on (a) Rh/MCM, (b) Pd/MCM, (c) Ru/MCM, and (d) Pt/MCM under the dark and UV irradiation conditions.

References

1   S. Wibowo, A. Yamaguchi, S. Shoji, T. Fujita, H. Abe and M. Miyauchi, *Chem. Lett.*, 2018, **47**, 935–937.

2   S. Shoji, A. Yamaguchi, T. Yamamoto, S. Matsumura, T. Fujita, X. Peng, H. Abe and M. Miyauchi, in *IPS-22 Conference*, Hefei, 2018.

3   H. Jiang, X. Peng, A. Yamaguchi, S. Ueda, T. Fujita, H. Abe and M. Miyauchi, *Sol. RRL*, 2019, **3**, 1900076.

4   O. Anjaneyulu, K. Takeda, S. Ishii, S. Ueda, T. Nagao, P. Xiaobo, T. Fujita, M. Miyauchi and H. Abe, *Mater. Chem. Front.*, 2018, **2**, 580–584.